Surface & Coatings Technology 493 (2024) 131266

Contents lists available at ScienceDirect

Surface & Coatings Technology

journal homepage: www.elsevier.com/locate/surfcoat

# Alumina coatings on Ni-based superalloys: The impact of annealing on heavy oil fouling

Fellipy S. Rocha [a,b,*], Etienne Bousser [c], Marwan Azzi [a], Fadila Khelfaoui [d], Luc Vernhes [d], Gregory S. Patience [b], Jolanta E. Klemberg-Sapieha [a], Ludvik Martinu [a,**]

[a] Department of Engineering Physics, Polytechnique Montréal, Montreal, QC H3T 1J4, Canada
[b] Department of Chemical Engineering, Polytechnique Montréal, Montreal, QC H3T 1J4, Canada
[c] Centre for Characterization and Microscopy of Materials, (CM)$^2$, Polytechnique Montréal, Montréal, QC H3T 1J4, Canada
[d] Velan Inc., 7007 Côte-de-Liesse, Montreal, QC H4T 1G2, Canada

ARTICLE INFO

*Keywords:*
Magnetron reactive sputtering
Thin film
Ni-based alloy
Alumina annealing
Mechanical properties
Heavy oil fouling and sulfidation

ABSTRACT

As the sweet crude oil reserves decline, refiners must treat sulfur-rich heavy oil, requiring harsher operating conditions, which are detrimental to process equipment. Application of coatings on critical components protects surfaces against sulfidation, corrosion, and fouling, extends the equipment's lifetime, and reduces the frequency of costly turnarounds. In the present work, we coated Inconel 625 and Inconel 718 substrates with amorphous alumina thin films at room temperature using reactive RF magnetron sputtering. Annealing of the deposited coatings at 800, 900, and 1000 °C increased hardness, improved adhesion, and generated crystalline polymorphs, predominantly γ-$Al_2O_3$ at lower temperatures, while α-$Al_2O_3$ was present at 1000 °C. The annealed substrates formed thermally grown oxides (TGOs), which interacted with the alumina coatings. The TGOs followed grain boundaries in the case of IN718 and a crater-like pattern on IN625. Annealed substrate precipitates generated columnar-like protrusions responsible for inducing crack propagation, which exhibited TGO formation. After 2 h exposure to heavy oil (containing 0.06 g $g^{-1}$ sulfur) at 450 °C and 11.3 MPa the as-deposited amorphous alumina presented no clear sign of adherent fouling, while the 1000 °C annealed crystalline alumina surfaces presented evidence of fouling.

## 1. Introduction

Nickel-based superalloys are the predominant choice for extreme environment applications involving high temperatures, and high mechanical stress [1], such as the petrochemical industry, aerospace, and power generation. Despite representing an evolution in applications at elevated temperatures, and being corrosion and creep resistant [2], the IN625 and IN718 alloys have been pushed to their operational limits, and their degradation is a significant concern in harsh environments. In the petrochemical industry, the alloys are subjected to fouling, a combined effect of reactions caused by sulfur and organic components from crude oil [3]. The deposition rate of either inorganic or organic material on the alloy surface depends on shear and temperature [4]. Temperature and reaction time rule the fouling reaction, which is the most significant cause of unstable reactor pressure control and valve failure [5]. With the depletion of conventional crude, heavy fractions are required to sustain the demand, which increases the amount of impurities and, consequently, sulfur content in the feed. Ebullated bed hydrocrackers are the most suitable reactors for processing this residual portion at temperatures above 350 °C, due to the catalyst replacement simplicity during operation [6]. Because of the extreme conditions, the fouling rate in these three-phase reactors is increasing, so materials with superior resistance to sulfidation and coke deposition are required.

Nickel-based alloys, especially when combined with chromium, control corrosion [7]. However, it has been well established that these alloys are prone to sulfidation, while $H_2S$ promotes their cracking [8]. The formed deleterious metal sulfide scales may act as a catalyst to form more sulfides in $H_2$-rich environments [7]. The continuous sulfide scales on the material surface have more defective structures when compared to oxidation. Thus, sulfidation rates are many orders of magnitude higher with faster diffusion pathways for the metallic cations [9]. Currently, there is no standardized quantitative data available for

* Corresponding author at: Department of Chemical Engineering and Engineering Physics, Polytechnique Montréal, Montréal, QC H3T 1J4, Canada.
** Corresponding author.
*E-mail addresses:* fellipy.rocha@polymtl.ca (F.S. Rocha), ludvik.martinu@polymtl.ca (L. Martinu).

https://doi.org/10.1016/j.surfcoat.2024.131266
Received 17 January 2024; Received in revised form 13 August 2024; Accepted 17 August 2024
Available online 23 August 2024

**Table 1**
Elemental composition of IN718 and IN625 provided by the supplier.

| Element | Limiting chemical composition, [wt%] | |
|---|---|---|
| | IN718 | IN625 |
| Ni | 50.0–55.0 | 58.0 min |
| Cr | 17.0–21.0 | 20.0–23.0 |
| Fe | Balance | 5.0 max |
| Nb + Ta | 4.75–5.50 | 3.15–4.15 |
| Mo | 2.80–3.30 | 8.0–10.0 |
| Ti | 0.65–1.15 | 0.40 max |
| Al | 0.2–0.8 | 0.40 max |
| Co | 1.0 max | 1.0 max |
| C | 0.08 max | 0.10 max |
| Mn | 0.35 max | 0.50 max |
| Si | 0.35 max | 0.50 max |
| P | 0.015 max | 0.015 max |
| S | 0.015 max | 0.015 max |
| B | 0.006 max | – |
| Cu | 0.30 max | – |

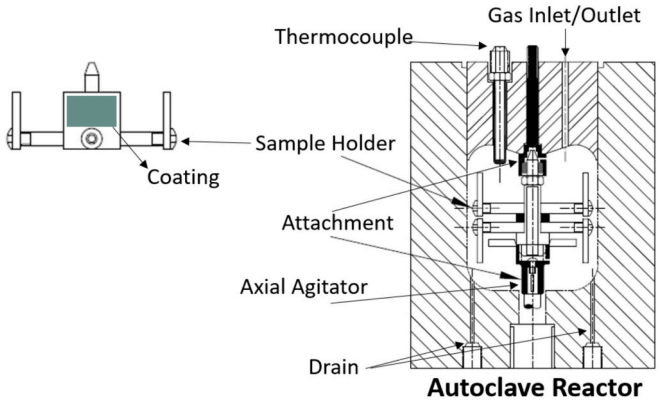


**Fig. 1.** Internal view of the batch reactor structure, and sample holder.

**Table 2**
Alumina coating deposited on glass: refractive index (*n*), *n*-gradient (%), extinction coefficient (*k*), and thickness obtained for different oxygen flow values.

| Power (W) | $O_2$ flow (sccm) | *n* | *n*-gradient (%) | *k* | Thickness (nm) | Deposition time (min) |
|---|---|---|---|---|---|---|
| 300 | 4 | 1.65 | 0.7 | 0.004 | 695 | 30 |
| 300 | 5 | 1.73 | 16 | 0.016 | 434 | 30 |
| 300 | 6 | 1.74 | 17 | 0.023 | 317 | 30 |

**Table 3**
Nanoindentation and scratch analysis of the alumina coatings deposited on IN625. The deposition time was increased for a higher $O_2$ flow rate to account for a lower deposition rate.

| $O_2$ flow (sccm) | *H* (GPa) (σ) | $E_r$ (GPa) (σ) | $H/E_r$ | $LC_1$ (N) | $LC_2$ (N) |
|---|---|---|---|---|---|
| 4 | 10.7 (0.9) | 193 (16) | 0.055 | 0.67 | 2.54 |
| 5 | 11.4 (0.5) | 188 (19) | 0.060 | 0.53 | 1.52 |
| 6 | 11.6 (0.8) | 186 (12) | 0.063 | 0.37 | 0.56 |

material comparison, hence the classification of material hot corrosion or sulfidation is typically qualitative and is often associated with the chromium content and chemistry of Fe-, Ni-, and Co-based alloys [10].

There is a need to achieve realistic simulated experimental conditions to validate the performance with respect to heavy oil fouling of candidate alloys and/or coatings. Unfortunately, the information

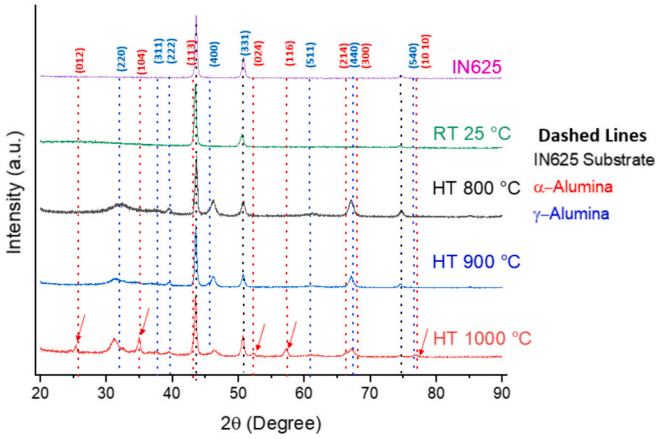


**Fig. 2.** XRD patterns of alumina coatings on IN625 before and after annealing. The dashed lines represent IN625 (black), γ-alumina (blue), and α-alumina (red). The corresponding alumina phases are indicated above the dashed lines. Database: α-$Al_2O_3$ (ICDD 046–1212) PDF-2, γ-$Al_2O_3$ (ICDD 002–1420) PDF-2.

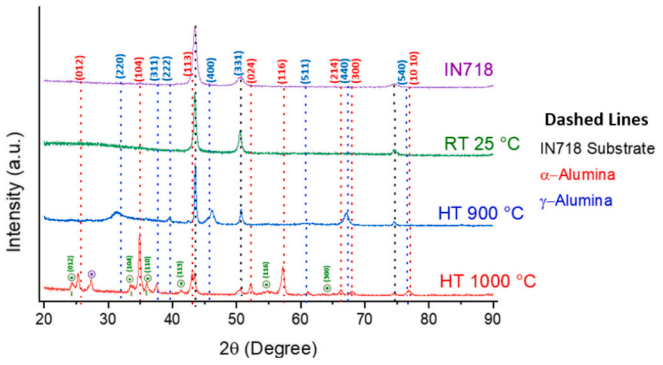


**Fig. 3.** XRD patterns of alumina coatings on IN718 before and after annealing. The dashed lines represent IN718 (black), γ-alumina (blue), α-alumina (red), and chromium oxide (green). The corresponding alumina phases are indicated above the dashed lines. Database: α-$Al_2O_3$ (ICDD 046–1212) PDF-2, γ-$Al_2O_3$ (ICDD 002–1420) PDF-2, and $Cr_2O_3$ (ICDD 038–1479) PDF-2. The dots correspond to $Cr_2O_3$ (green), and $NbCrO_4$ (purple).

available about materials performance under real-life conditions is scarce and sparse with a wide range of specifications [11]. The results are often difficult to interpret precisely, and they present apparent contradictions in understanding the possible mechanisms [12]. Thin film technology represents a promising solution to the challenge of protecting the surface of superalloys while maintaining their bulk properties. A coating composition can be chosen exclusively for the desired environmental protection, without the constraints of designing alloys to preserve the structural integrity under extreme conditions [13]. Physical Vapor Deposition (PVD) offers an environmentally friendly and safe deposition process. More precisely, magnetron sputtering allows for effective control of the coating composition, thickness, grain size, and orientation. Thus, it is possible to achieve high hardness, chemical resistance, low porosity, good adhesion and relatively high deposition rates [14]. In the context of protection against oxidation, sulfidation and fouling, oxides are typically considered to decrease surface reactivity.

Alumina ($Al_2O_3$) has many metastable polymorphs that are categorized as face-centred cubic (FCC) and hexagonal closed-packed (HCP) structures. Alpha alumina (corundum) is a thermodynamically stable form and is arranged in an HCP trigonal lattice [15]. Based on aluminum-containing alloy results, $Al_2O_3$ is expected to provide the best possible protection against sulfur corrosion [16]. However, the formation of a continuous layer of alumina from alloy oxidation requires a

**Table 4**
Elasto-plastic properties before and after annealing of alumina deposited with an oxygen flow rate of 4 sccm on IN625 and IN718 substrates. The critical load values constitute the cohesive ($LC_1$) and adhesive ($LC_2$) strength of the films.

| Substrate | Annealing temperature | $H$ (GPa) | Stdev $H$ | $E_r$ (GPa) | Stdev $E_r$ | $LC_1$ [N] | $LC_2$ [N] |
|---|---|---|---|---|---|---|---|
| IN625 | As-deposited | 10.7 | 0.9 | 192.5 | 15.7 | 0.82 | 2.54 |
| | 800 °C | 21.1 | 1.0 | 265.5 | 12.4 | 1.09 | 4.23 |
| | 900 °C | 21.7 | 2.2 | 262.8 | 22.3 | 1.56 | 4.70 |
| | 1000 °C | 20.6 | 1.7 | 247 | 19.9 | 4.92 | 6.32 |
| IN718 | As-deposited | 11.1 | 0.4 | 198.4 | 7.6 | 0.62 | 2.09 |
| | 900 °C | 21.2 | 1.3 | 256.6 | 9.8 | 1.49 | 4.03 |
| | 1000 °C | 20.6 | 2.0 | 306.3 | 41.1 | 4.07 | 6.33 |

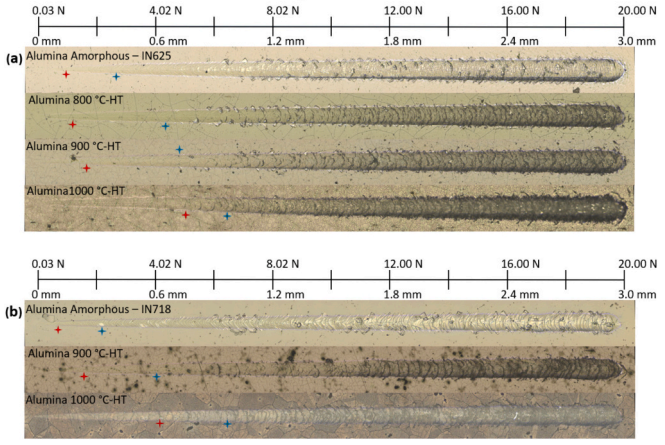


**Fig. 4.** Scratch tracks of alumina coatings deposited on IN625 (a) and on IN718 (b) before and after annealing at 800, 900, and 1000 °C for 2 h. The cohesive failure ($LC_1$) is marked in red, and the coating adhesion failure ($LC_2$) is marked in blue.

higher aluminum content [16]. Direct deposition of thin alumina films on metallic substrates has been reported using various PVD methods. Generally, the thin film is amorphous at a temperature lower than 500 °C, while higher substrate temperatures during deposition, and post-deposition annealing favor metastable polymorphs [17]. To create an alumina crystalline phase by reactive magnetron sputtering (e.g., radiofrequency (RF) sputtering), higher substrate temperatures are required: 500 °C to obtain γ-$Al_2O_3$, and 700 °C to obtain α-$Al_2O_3$ [18]. Crystalline alumina, especially α-alumina, provides a barrier against the direct migration of metallic elements (e.g., Fe, Ni, and Cr) from the substrate alloy to the surface at elevated temperatures [19]. Crystalline alumina is best suited for applications related to wear, as it tends to be harder than the amorphous phase. Although significant progress has been made in fabricating crystalline alumina by PVD, the simplest approach to produce the alpha phase is a deposition of an amorphous alumina layer at room temperature followed by annealing above 900 °C.

Annealing is prohibitive for many temperature-sensitive substrates inducing unwanted microstructural changes, delamination due to incompatible coefficients of thermal expansion (CTE), and permanent macro deformation of the components. Moreover, while considering thin film technology, one must always keep in mind substrate effects, especially for high-temperature applications where diffusion of the substrate material into the coating matrix is expected. Investigation of alumina coating performance with the influence of the substrate is very important with the aim to develop a dense, defect-free, amorphous coating that would protect the substrate by limiting sulfur diffusion, which occurs mainly through grain boundaries and porosity, along with superficial sulfide scale formation [20]. Besides the surface chemistry and microstructure, the coating thickness is an important factor in providing protection [21]. Previous studies demonstrated that an ALD-deposited alumina passive layer of 5 nm was sufficient to protect against heavy oil fouling at 350 °C. However, the $Al_2O_3$ layer delaminates after heavy oil fouling tests at high pressure and 350 °C [22]. Above 350 °C, the fouling process initiates via the decomposition of sulfur-containing molecules forming hydrogen sulphide ($H_2S$), which reacts with metals, and coke forms a strongly adherent carbonaceous and brittle metal-sulfide film on the surface [23].

This article focuses on investigating the performance of alumina thin films deposited at room temperature using the RF reactive magnetron sputtering technique as a fouling resistant coating. We study the effect of annealing on the microstructure of amorphous alumina on IN625 and IN718. Different metastable polymorphs of alumina are formed, with γ-$Al_2O_3$ and α-$Al_2O_3$ being the predominant crystalline phases. We show that the fouling resistance varies with the alumina microstructure, while its amorphous phase exhibits the best performance, with no clear sign of adherent fouling. Unlike other published studies, in this work, we did not observe any coating delamination after fouling up to 450 °C.

## 2. Materials and methods

### 2.1. Surface preparation and coating deposition

Surface preparation affects the surface's ability to form durable well-adhering coatings as it removes weak boundaries and contamination [24]. It consisted of two steps:

A. *Substrate polishing:* IN718 and IN625 coupons (25 × 25 × 3 mm) were polished using SiC paper (grit sizes from 240 to 800), followed by diamond particle suspension (from 9 μm to 1 μm), and finally a colloidal alumina suspension. Before deposition, the substrates were sequentially cleaned in acetone and then isopropanol ultrasonic bath. The elemental composition of IN625 and IN718 is presented in Table 1.

B. *Sample mounting and pre-treatment:* The coupons were mounted on a 150 mm diameter sample holder. A plasma sputter-cleaning process was applied for 30 min in Ar at 5 mTorr (0.67 Pa) and an RF-induced negative bias of −650 V. This step removes the native oxide layer from the surface, while also promoting surface activation and consequently chemical reactivity [25].

The deposition system consisted of a 30 L vacuum chamber evacuated by mechanical and turbomolecular pumps. The magnetron head holding a 50 mm diameter Al target (99 % purity) from Kurt J. Lesker was connected to a Seren RF power supply. Another Seren RF power supply was connected to the sample holder (150 mm diameter) to control the bias voltage, which was applied to the substrate only during the pre-treatment step. The alumina was deposited at various oxygen flow rates (4, 5, and 6 sccm) while keeping the Ar flow rate constant (35 sccm). The chamber pressure during deposition was 5 mTorr.

After pre-treatment, Ar plasma was ignited at the magnetron, while the shutter was closed, to clean the target until the bias voltage generated by the plasma stabilized. Oxygen was then introduced into the chamber, and the shutter was kept closed until the bias stabilized again, signaling that the target had reached a suitable composition (due to

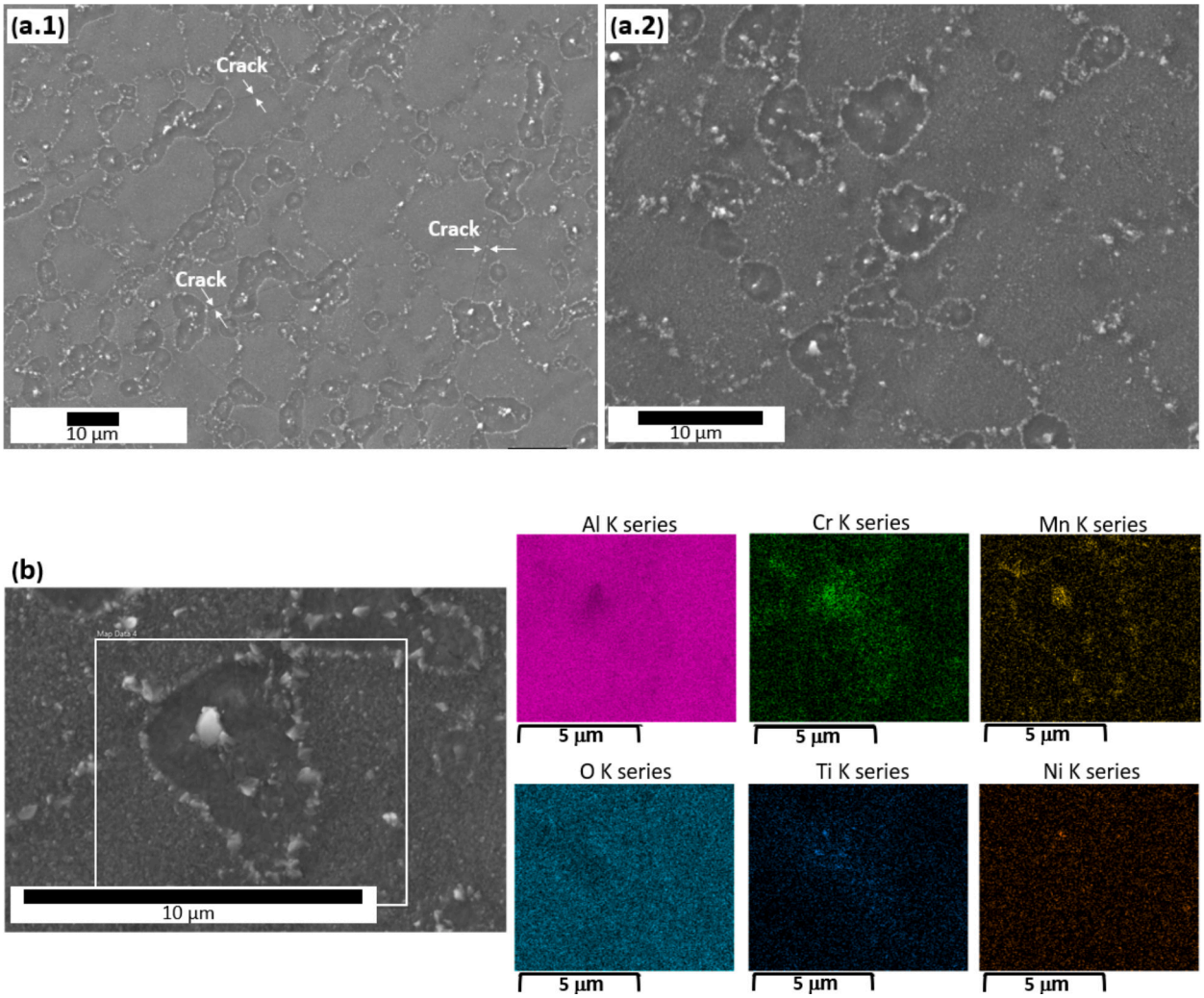


**Fig. 5.** SEM images and EDS compositional maps of the surface of alumina-coated IN625 after annealing for 2 h at 1000 °C. EDS maps correspond to the highlighted rectangular area.

poisoning). Deposition started when the target bias stabilized and the shutter was opened. The substrate temperature was maintained at ambient without the application of external heating or cooling, and the substrate rotation speed was set at 55 rpm. The total RF power applied to the target was 300 W for the deposition on both metal substrates. The coatings on the Inconel substrates had a thickness of approximately 1.5 µm.

After deposition, the coated samples were annealed in a Carbolite furnace in air at 800 °C, 900 °C, and 1000 °C, for 2 h, at a heating rate of 60 °C/min. Following annealing, the samples were let to cool down in the furnace after the power was interrupted, and they were retrieved the next day.

### 2.2. Coating characterization

#### 2.2.1. Ellipsometry

Variable angle spectroscopic ellipsometry was used to assess the coating thickness and the refractive index changes throughout the thickness for films deposited on soda-lime glass. The RC2 ellipsometer from the J.A. Woollam Co. is equipped with two rotating compensators. The measurements were performed at several angles of incidence 45°, 55°, 65°, and 75° in a wavelength range from 200 nm to 1700 nm. An optical model was created based on the Tauc-Lorentz and Gaussian oscillators using the CompleteEase software. The refinement of the optical model provided information about the thickness and surface roughness of the layer, refractive index dispersion curves, and the possible presence of anisotropy.

#### 2.2.2. Microscopy

A scanning electron microscope (SEM, JEOL JSM-7600F) equipped with an Oxford Instruments X-Max energy dispersive X-ray spectroscopy (EDS) detector was used to assess the film thickness, microstructure, topography, and elemental composition. Focused Ion Beam (FIB) system (Hitachi FB-2000A) with $Ga^+$ ions was used at 30 kV to prepare cross-sections of the coated samples after annealing. The trench produced by FIB enabled one to observe the microstructure by SEM at a 45° angle. The real dimensions of the observed microstructures on the FIB-prepared samples are smaller than those on the micrographs because of the 45° cut angle.

#### 2.2.3. X-ray diffraction

X-ray diffraction (XRD) measurements were carried out using a Bruker Discover D8 X-ray diffractometer in a grazing angle geometry with Cu Kα radiation (8.04 keV) in a parallel beam configuration with a Gobel mirror (incident beam optics) and Soller slits (diffracted beam optics). The selected grazing angle was $\alpha = 1.0°$ for all measurements, and the range of the $2\theta$ hkl scans was from 20 to 90°.

#### 2.2.4. Micro-scratch testing

A Micro Combi Tester (MCT3, Anton Paar, Graz, Austria) equipped

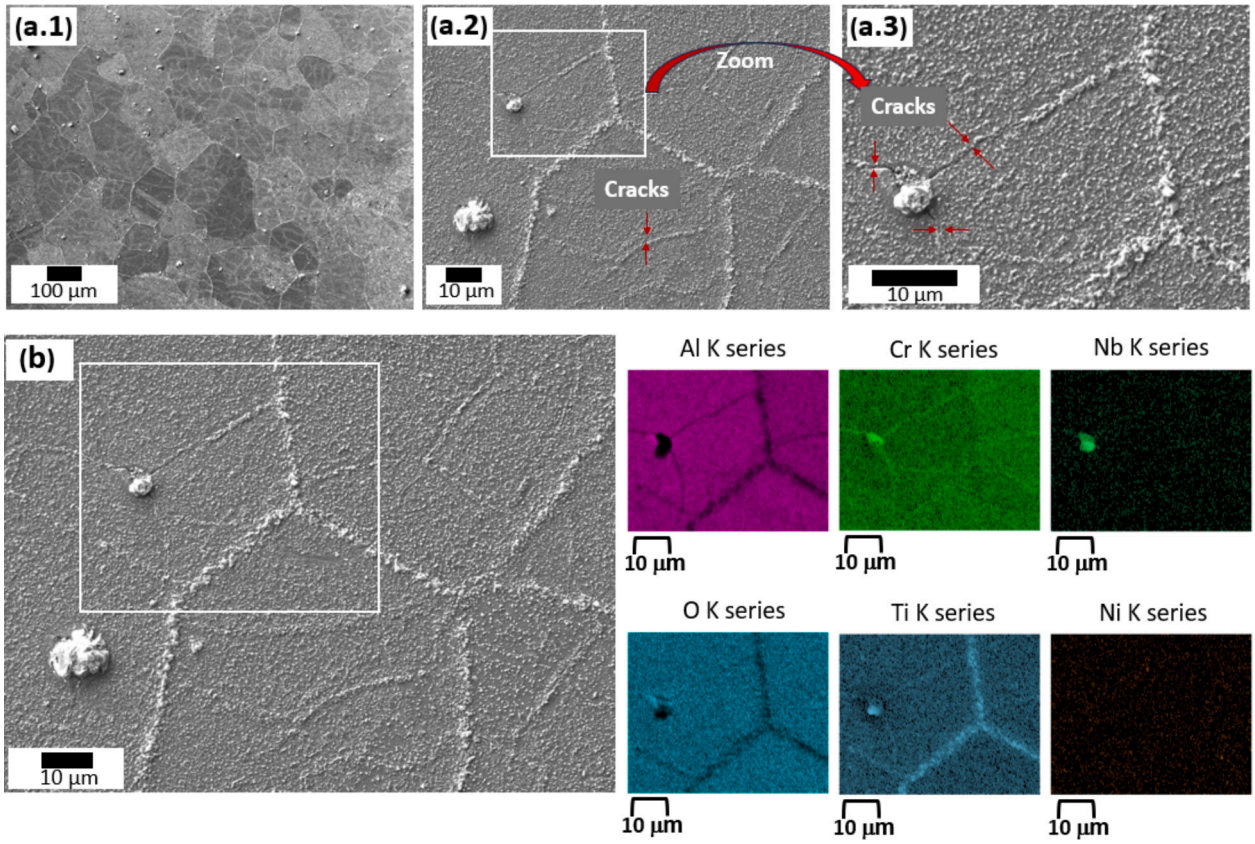


**Fig. 6.** SEM images and EDS compositional maps of the surface of alumina-coated IN718 after annealing for 2 h at 1000 °C. EDS maps correspond to the highlighted rectangular area.

with a 200 µm radius Rockwell diamond tip was applied to measure the adhesion of alumina films. The test consisted of a progressive load increasing from 0.03 to 20 N over a scratch length of 3 mm at a speed of 6 mm/min. The critical load 1 ($LC_1$), which corresponds to a cohesive tensile failure, was determined as the normal force where the first crack occurred. The coating adhesion or critical load 2 ($LC_2$) was associated with the load at which the coating delaminates. The scratch tracks were observed post-mortem by optical microscopy. The $LC_1$ and $LC_2$ values were identified following the ASTM C1624 standard. At least two scratches were performed for each sample to ensure reproducibility. The results presented in the paper show the most representative data.

#### 2.2.5. Nanoindentation

A depth-sensing indentation instrument (Hysitron Inc. – Bruker TriboIndenter) equipped with a Berkovich pyramidal tip was used to determine the hardness ($H$) and reduced Young's modulus ($Er$) of the coatings. The area function of the tip was calibrated using a fused silica standard. All measurements were performed with multicycle progressively increasing load indentations with loads ranging from 1 to 200 mN. Each sample was tested using a 4 × 4 indentation matrix and the properties were calculated from a minimum of 25 indentations per spot. Each unloading cycle was analyzed using the Oliver and Pharr method [26], while coating hardness and modulus were determined using the methodology proposed in the ISO 14577-4 standard. The $H$ and $Er$ values are extracted from a plateau region independent of the penetration depth and the indentation tip effects.

### 2.3. Fouling test

For the fouling tests, the samples were positioned vertically to mitigate gravitational effects in an autoclave-type reactor (see Fig. 1) filled with 200 g of heavy oil containing 6 wt,% sulfur. The system was pressurized with argon up to 11.3 MPa controlled by a backpressure regulator and purged for 5 min to evacuate any oxygen. The temperature cycle in the vessel consisted of 2 h of temperature increase to reach an internal temperature of 450 °C, followed by a hold time of 2 h to ensure that all heavy oil cracked, after which the system was allowed to cool until the next day before depressurizing, opening, and retrieving the samples. The recovered samples were washed with a 50:50 solution of petroleum ether and toluene, followed by a water rinse to remove non-adherent material. The samples were dried in the air and stored before subsequent analyses.

## 3. Results

### 3.1. Alumina deposition optimization

In the first series of experiments, amorphous alumina films were prepared on glass and IN625 substrates using argon and varying oxygen flow rates in the hysteresis transition zone with a deposition time of 30 min. Hysteresis is a non-linear change in operation conditions caused by poisoning due to compound formation on the target during reactive magnetron sputtering [27]. Hence, there is a need for optimization, which was achieved through monitoring the films' optical (Table 2), and elasto-plastic (Table 3) properties.

The refractive index ($n$) slightly increased with higher $O_2$ flow rate and power (between 1.65 and 1.74 @ 550 nm), while the extinction coefficient ($k$) varied between 0 and 0.02, pointing out the near-stoichiometry of the deposited alumina layers. The stability of the growth process has been assessed based on the refractive index ($n$) gradient throughout the coating. The variation of $n$ ranged from 0 % to 17 % throughout the coating thickness. The alumina films deposited with an $O_2$ flow of 4 sccm possessed the lowest $n$-gradient, signifying the highest level of homogeneity. At this condition, the obtained thickness

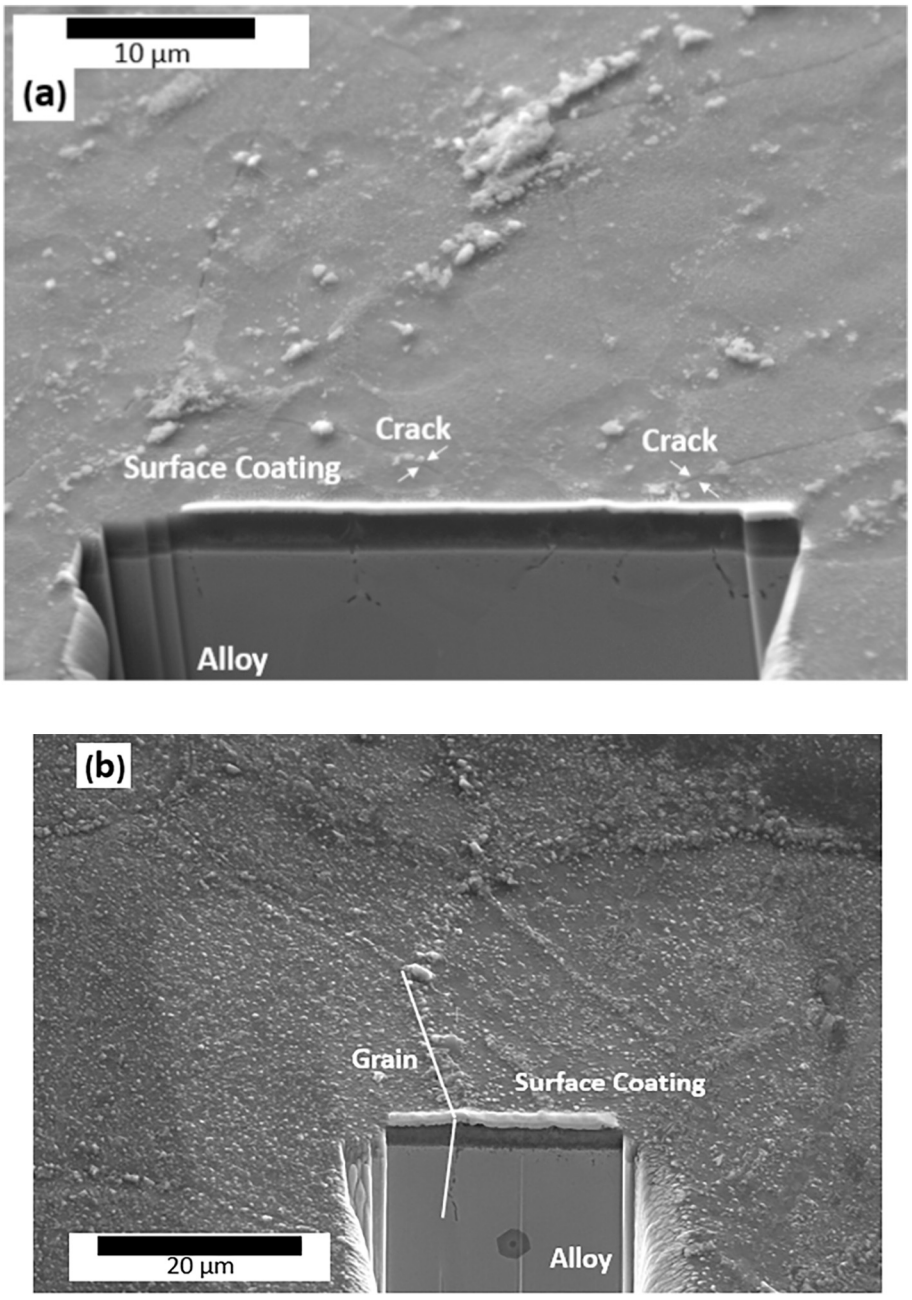


**Fig. 7.** Surface region showing the FIB cut area in the alumina-coated IN625 (a) and IN718 (b) after annealing for 2 h at 1000 °C. The surface is angled by 45° to show the correspondence between the surface and coating/substrate interface. It is possible to identify the correspondence of the alumina grain boundary with the grain boundary of the substrate for IN718 (indicative lines), but no correspondence of the surface grain boundary is present for the IN625.

was also higher, indicating a higher deposition rate, characteristic of a sputtering process regime at the boundary between the metallic and poisoned modes [28].

EDS measurements confirmed a slightly sub-stoichiometric composition of the as-deposited films (oxygen concentrations of 61 %, 62 %, and 63 % for 4, 5, and 6 sccm of $O_2$, respectively). These values are not affected by the substrate since the complete volume of interaction is within the 1.5 µm thick coating; in fact, the used electron acceleration voltage of 10 kV corresponds to a volume of interaction determined by a penetration depth of ~0.85 µm for a reference $Al_2O_3$ layer using the Kanaya-Okayama formula [29].

Analysis of the elasto-plastic properties (Table 3) indicates that the hardness and the $H/E_r$ ratio slightly increased while Young's modulus slightly dropped when increasing the oxygen concentration. The $LC_1$ and $LC_2$ values from the micro-scratch test (Table 3) confirm that the film deposited with 4 sccm of $O_2$ is more scratch-resistant and adheres better. In addition, this film also possesses the lowest $n$ gradient, suggesting that higher coating homogeneity is indicative of better adhesion performance.

### 3.2. Effect of annealing

#### 3.2.1. Film crystallinity

In the second series of experiments, conducted after the process and amorphous alumina coating optimization, we deposited films for the subsequent annealing study at a flow rate of 4 sccm of oxygen. This choice was based on better homogeneity, higher deposition rate, and superior adhesion and cohesion. It should be noted that indexing XRD

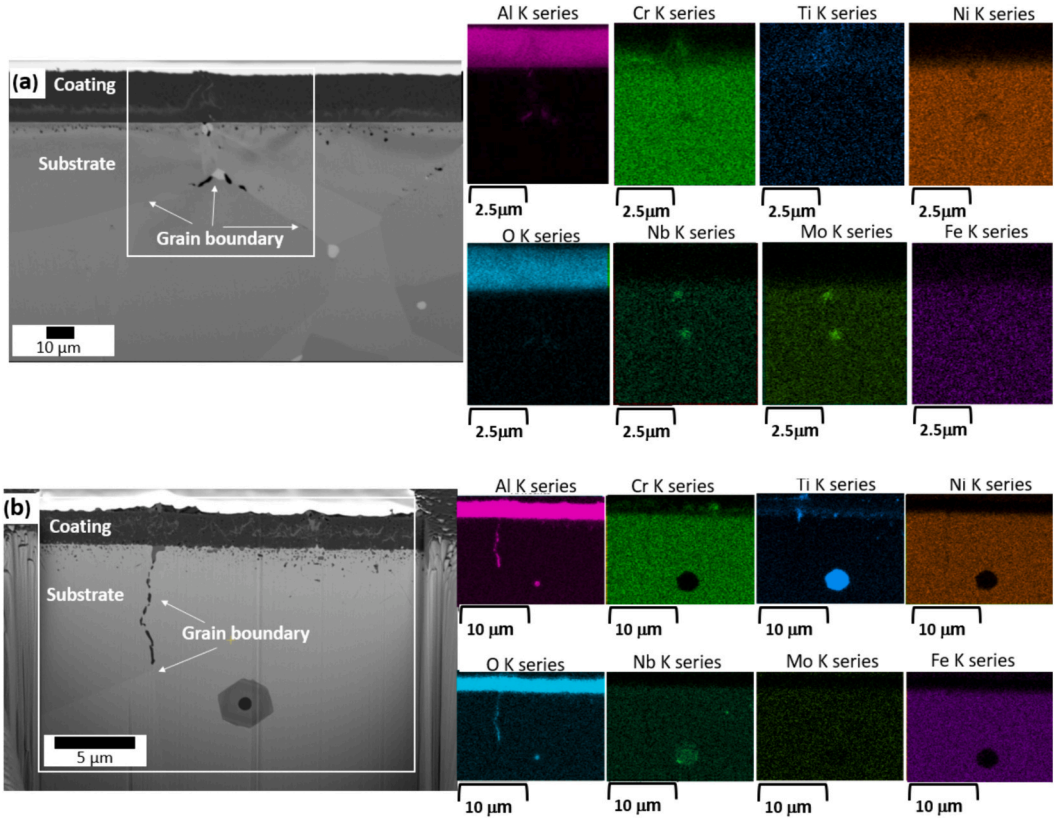


**Fig. 8.** FIB SEM cross-sections and EDS maps of alumina-coated IN625 (a) and IN718 (b) after annealing at 1000 °C for 2 h. EDS maps correspond to the highlighted rectangular areas.

patterns from annealed multi-element alloys is challenging because multiple candidate phases can overlap. In general, the oxidation of nickel-based alloys gives rise to chromium oxides, delta-phase ($Ni_3Nb$) precipitates, inner oxides, voids, and pores [30]. However, in the case of the diffractograms presented below, the alumina allotropes gave the highest confidence results.

The as-deposited coatings are amorphous, as the XRD diffractogram at room temperature only shows peaks due to the substrate IN625 (Fig. 2), and IN718 (Fig. 3). After annealing IN625 at 800 °C, the main peaks correspond to γ-$Al_2O_3$ formation. The latter peaks further sharpen at 900 °C, while the peaks at 37° and 61° disappear, and the peak at 32° shifts to the left, which represents the formation of additional alumina transition phases, possibly δ and θ [15]. Finally, the sample annealed at 1000 °C exhibits peaks corresponding to α-$Al_2O_3$. However, the peaks from γ-$Al_2O_3$ are still visible, and the peak at 32° is now narrower, slightly shifted, and more prominent.

Similar to IN625, films on IN718 also confirm the formation of γ-$Al_2O_3$ at 900 °C. (Fig. 3**)**. However, when annealed at 1000 °C, all γ-$Al_2O_3$ peak heights are drastically reduced, and the peaks corresponding to α-$Al_2O_3$ become dominant. In addition, peaks ascribed to the formation of $Cr_2O_3$ are now visible, indicating a higher degree of diffusion of chromium into the alumina film. This enhances the formation of α-$Al_2O_3$ since $Cr_2O_3$ is a known template to induce alpha alumina formation due to their lattice compatibility [31].

### 3.2.2. Mechanical properties

The mechanical properties of the alumina coatings before and after annealing are summarized in Table 4. The hardness has approximately doubled after annealing due to crystallization, with a maximum value over 21 GPa for the coatings deposited on IN625 and IN718 and annealed at 900 °C. The H values became slightly lower (20.6 GPa) for samples annealed at 1000 °C. The results of the micro-scratch testing suggest that the cohesive properties and adhesion improve after annealing the films for both substrates (see Fig. 4 and Table 4). The $LC_1$ values for alumina on IN625 are systematically higher than those on IN718. The $LC_2$ results for alumina on IN625 are initially higher, but they are equivalent to 6.3 N for both substrates after annealing at 1000 °C.

### 3.2.3. Surface analysis

To better understand the effect of annealing on the alumina coatings and the alumina/Inconel systems, SEM and EDS measurements were performed on the surface and cross-sections of samples annealed at 1000 °C. The EDS surface analysis was conducted with a 5 kV accelerating voltage to ensure a superficial analysis and avoid substrate interference. The acceleration voltage during the cross-section EDS analysis was varied from 5 kV to 25 kV. The most revealing imaging conditions were generated at 15 kV; specifically, the images at 15 kV presented a better identification of Ti diffusion and enhanced Cr resolution. At 5 kV, Cr is detectable only by the Lα (0.572) line, which can convolute with the O Kα (0.525) line, possibly leading to interpretation errors.

As-deposited amorphous alumina films are typically smooth with a roughness on the nanometric scale, in agreement with the literature [32]. The microstructure of alumina coatings on IN625 after annealing at 1000 °C is illustrated in Fig. 5. The surface appears to be covered by circular crater-like structures with tower-like protrusions inside the craters (see Fig. 5a), without any clear pattern. Further EDS analysis (Fig. 5b) indicated that the borders of the crater-like structures are rich in Mn, while the protrusions and the internal part of the craters are rich in Cr, Ti, and Mn. We found that after annealing the alumina-coated IN625 at 1000 °C, only Ni, Mn, Cr, and Ti diffuse (Fig. 5b), consistent with the previous studies [34].

IN718 has an elemental composition similar to IN625, but with higher concentrations of Ti, Al, and Nb, and lower concentrations of Mn,

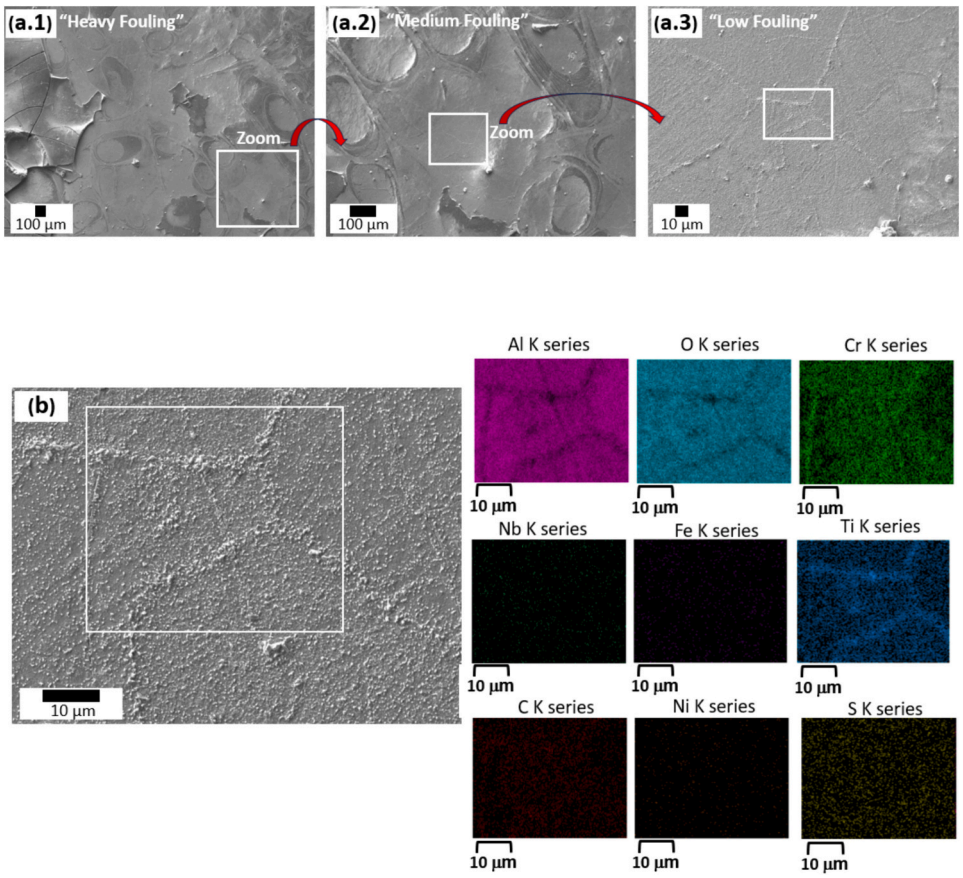


**Fig. 9.** Alumina-coated IN718 after annealing for 2 h at 1000 °C followed by heavy oil fouling for 2 h at 450 °C: a) SEM images of representative areas at different magnifications; b) Magnified SEM image of the rectangular section of (a.3) and corresponding EDS maps.

Si, Mo, Cr, and Ni (see Table 1). The annealed alumina film on IN718 (Fig. 6a) indicates two types of delimitation lines, a thicker one and a thinner one. The thinner lines are interpreted as cracks, more evident in the higher magnification image, and the thicker lines coincide with grain boundary-like regions, evidenced by the image contrast. The TGO surface pattern matching the substrate grain boundaries is consistent with the literature [33,34]. The EDS results (Fig. 6b) of the alumina-coated IN718 after annealing indicate that the thickness of the lines is related to the amount of elemental diffusion. The TGO over the grain boundary region is thicker due to a facilitated diffusion. From the EDS results (Fig. 6b), we can see a deficit of aluminum in all lines on the surface, while Cr and Ti predominate. The tower-like protrusions are mainly formed by Nb, Ti, and Cr from the substrate material.

### 3.2.4. *FIB cross-section analysis*

In the following, we performed a detailed analysis of the FIB cross-sections (Fig. 7 and Fig. 8) to assess the correspondence of the TGOs seen in the coating surface by SEM in Fig. 5 and Fig. 6 and the substrate microstructure. In this case, Fig. 7 angled images show the area surrounding the FIB cuts. No alignment between IN625 grains and alumina surface structures has been observed; in Fig. 7a, only the crater-like structures can be detected, together with protrusions and small cracks. In contrast, the grain boundaries of the IN718 substrate are aligned with the thicker lines on the coating surface (see Fig. 7b) as also indicated in Section 3.2.3.

SEM and EDS analyses of the cross-sections of the alumina-coated IN625 (Fig. 8a) and IN718 (Fig. 8b) present a similar behavior close to the substrate-thin film interface. After annealing, the substrate region near the interface exhibits structures characteristic of Kirkendall porosity. This type of porosity represents the removal of alloying elements from the substrate matrix while forming TGOs. Ti and Cr diffuse into the alumina layer and accumulate in the substrate/coating interface, forming a gradient mixed layer, which might be responsible for the adhesion improvement. For Ni—Cr alloys, the voids are due to the simultaneous diffusion of Cr and Ni. Specifically, the diffusion kinetics in the chromium removal zone dictates the formation of voids [35]. Since Cr diffuses faster than Ni and when a net flux of vacancies is established, the condensation of the vacancies contributes to void formation and/or their growth [36].

### 3.3. *Heavy oil fouling on alumina-coated inconel surfaces*

To obtain more insight into the interaction of the heavy oil during the fouling experiments, we studied both types of annealed substrate-coating systems by lower magnification SEM images (Fig. 9a and Fig. 10a). The samples exhibited areas with carbonaceous materials in the form of islands with structural differences. For IN718 (Fig. 9a), outside the area completely covered by coke, the sample is similar to the one without fouling (Fig. 6a**).** When analyzing the EDS data from the alumina-coated IN718 after fouling (Fig. 9b), it is noticeable that the surface is similar to the samples before fouling (Fig. 6b**).** Besides this similarity, after fouling, it exhibits a lower concentration of Ti and Cr in the grain boundary regions, leading to a possible interaction of these areas with the heavy oil during the hydrocracking reaction. A small amount of carbon is evenly distributed on the alumina-coated IN718 after fouling. A weak, evenly distributed sulfur signal was detected, which is expected to arise from the sulfur present on the adherent carbonaceous material. No clear sign of sulfidation was detected on the coated IN718.

For IN625 (Fig. 10) after fouling, the cracks became more visible and

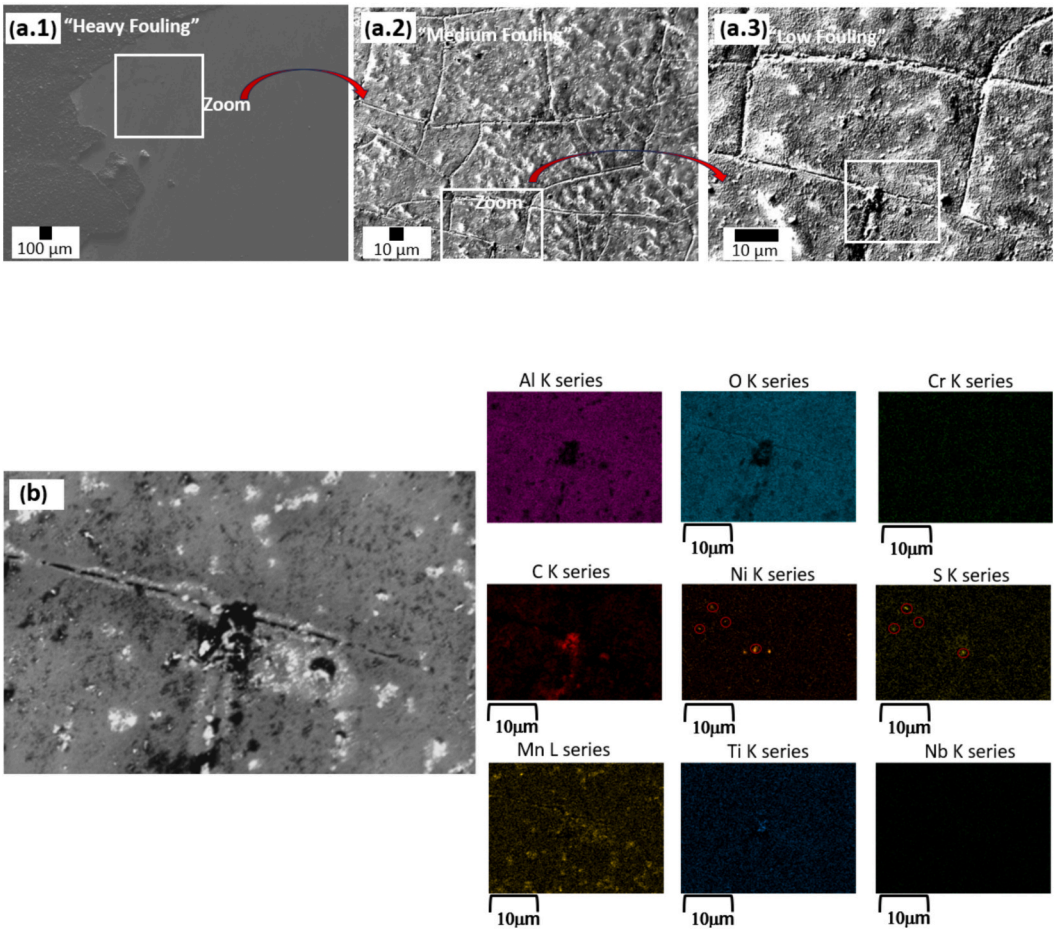


**Fig. 10.** Alumina-coated IN625 annealed for 2 h at 1000 °C followed by heavy oil fouling for 2 h at 450 °C: a) SEM images at different magnifications, and b) Magnified SEM image of region (a.3) and corresponding EDS maps.

deeper, clearly with less TGO than the surface of the IN718 sample (Fig. 9). In addition, the alumina-coated IN625 surface after fouling (Fig. 10a) does not indicate the characteristic crater-like structures observed prior to fouling (Fig. 5). The EDS maps of the cross-section of alumina-coated IN625 (Fig. 10b) confirm that the cracked region is mainly void, and carbon and sulfur are present in the cracked area.

Analysis of the FIB-prepared cross-sections after fouling provides complementary information about the possible diffusion of sulfur and carbon toward the substrate. For the FIB cut, we chose a location that contained coke islands and visible grain boundaries for IN718 (Fig. 11a.1), and a crack for IN625 (Fig. 11b.1). Here, we did not observe any internal diffusion of S or C for either one of the coated substrates. Comparing the EDS results from samples before and after fouling, no differences in patterns of elemental diffusion could be discerned for IN718 (Fig. 11a.2).

The protection against fouling of the as-deposited alumina was also tested. The cross-section of alumina-coated IN718 (Fig. 12a) and IN625 (Fig. 12b) shows no adherent layer on their surface. The EDS maps indicate no elemental diffusion from the alloy or sulfur infiltration in the coating matrix. Both as-deposited coating systems effectively protected the surface against the formation of scales and the deposition of carbonaceous material.

## 4. Discussion

The coatings were optimized and deposited on the nickel alloys in an amorphous state. The properties of the substrates, such as hardness, elastic modulus, and thermal characteristics, also affect the properties of the PVD coatings [37]. The H and Er values for as-deposited and annealed coatings on IN718 and IN625 are comparable within the experimental error (see Table 4). The substrates may cause possible changes in the coating residual stress, affecting the mechanical behavior such as fracture toughness and adhesion [38]. The as-deposited alumina adhesion on IN625 is about 20 % higher than the adhesion on IN718. However, the coating adhesion increased on both substrates after annealing, reaching equivalent $LC_2$ values at 1000 °C, thus increasing 3 times for IN718 and 2.5 times for IN625. The improvement of adhesion after annealing can be related to the formation of TGO at the interface.

The uncoated alloys oxidation is characterized by the formation of $Al_2O_3$ at the grain boundaries, Ti oxides at the scale-alloy interface, main scale containing Cr, Nb, $(Mn,Cr)_3O_4$ spinel, and metal carbide precipitates [39,40]. The coating affected the oxidation of the alloys, where the expected Nb oxide layer was not observed, and Mn diffusion was observed only for IN625. Accumulation of Cr and Ti at the substrate-coating interface was observed in both IN625 and IN718 (Fig. 8). Chromium- and titanium-derived TGO can improve alumina adhesion due to the interface enrichment with Ti and Cr oxide [39]. Ti has a high interaction energy with alumina, and the adhesion energy to separate $Cr_2O_3$ from $Al_2O_3$ is higher than the alumina cohesion energy [41]. The titanium concentration on annealed IN718 is prominent, attributable to a higher Ti content (1 % in IN718 compared to 0.4 % in IN625 – Table 1). The possible formation of manganese spinel decreases the evaporation and formation rate of volatile Cr-species [42]. Thus, manganese structures formed on IN625, reducing the $Cr_2O_3$ formation.

During annealing, the coatings undergo phase transformation and show polymorphism (Fig. 2 and Fig. 3). The volume change associated

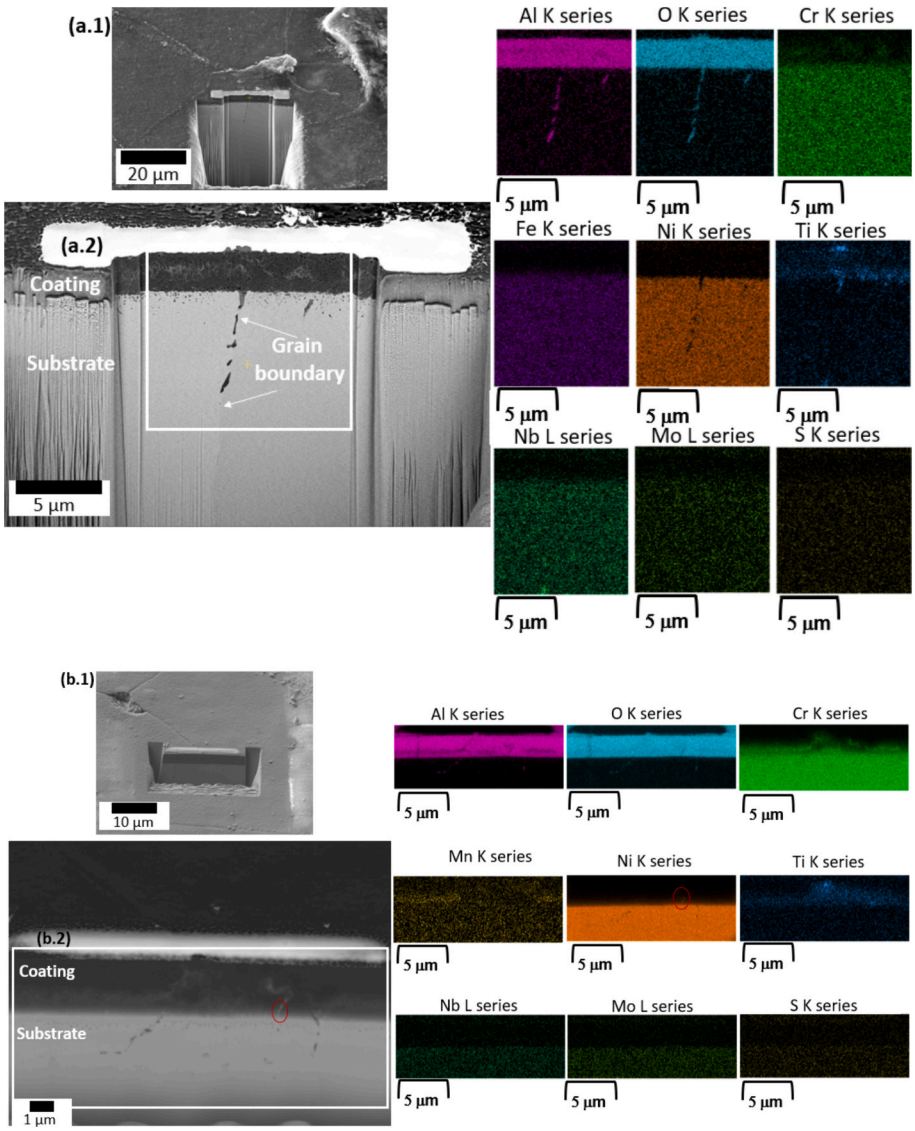


**Fig. 11.** SEM images and EDS maps on the FIB-prepared cross-sections of alumina-coated IN718 (a) and IN625 (b) samples after annealing at 1000 °C for 2 h followed by fouling at 450 °C for 2 h. Images a.1 and b.1 show the surface of the cut area, and EDS maps are taken from the highlighted rectangular areas in a.2 and b.2.

with the alumina phase transformation combined with CTE mismatch generate stress that can relax through defect formation, indicated by the cracks seen in Fig. 5 and Fig. 6. For example, the transformation of the γ-$Al_2O_3$ cubic phase (density, $d = 3.56$ g cm$^{-3}$) to α-$Al_2O_3$ hexagonal phase ($d = 3.98$ g cm$^{-3}$) results in a volume reduction of approximately 10 % and a large increase in density [43]. The coating thickness, heating rate, and grain size may affect microstructural changes during annealing. Specifically, it has been shown that the α-$Al_2O_3$ phase formation at 1000 °C dominates for sputtered coatings over a threshold thickness of 1.2 µm [44]. The annealing of amorphous sputtered films at heating rates above 25 °C/min contributes to the formation of thermodynamically demanding phases [45]. Therefore, in our case, with films of about 1.5 µm and a heating rate of 60 °C/min, the conditions favor the formation of the α-$Al_2O_3$ phase.

TGO is present on the surface of the coatings and is characterized by a granular microstructure (Fig. 5 and Fig. 6). A higher quantity of TGO forms in the coating defect regions, providing a "short-circuit path" through the coating to the surface, enabling faster diffusion. The tower-like protrusion growth induced the formation of more defects in the coating structure. Oxidation of NbC precipitates to $Nb_2O_5$ has been shown to create tower-like protrusions [33,46,47]. In addition, the compressive stress caused by the formation of alumina and other inner oxides in certain regions (such as seen in Fig. 8) could help induce the material ejection from the grain boundaries and formation of TGO. The formation of aluminum oxides inbetween the grains deep in the IN718 and IN625 alloy matrices has been pointed out by several authors [30,35,39].

In our experiments, the sensitivity of the alumina-coated Inconel substrates to fouling has been tested at a temperature of 450 °C over 2 h, to induce the thermally-activated reaction of aliphatic sulfur compounds from heavy crude oil that forms hydrogen sulfide. In the fouling testing reactor, complex environments susceptible to the exposure of combined hot gases emanating from the oil ($H_2$, CO, $CO_2$, $H_2$, and $H_2S$) have an increased number of reaction pathways to degrade the coating and the substrate. The protectiveness of the coating system against fouling depends on surface passivation. Alumina can be considered immune to oxygen environments [48], and has shown to be resistant to sulfidation [16,22].

Neither the as-deposited alumina nor the annealed system showed signs of delamination after the fouling tests for both substrates. No

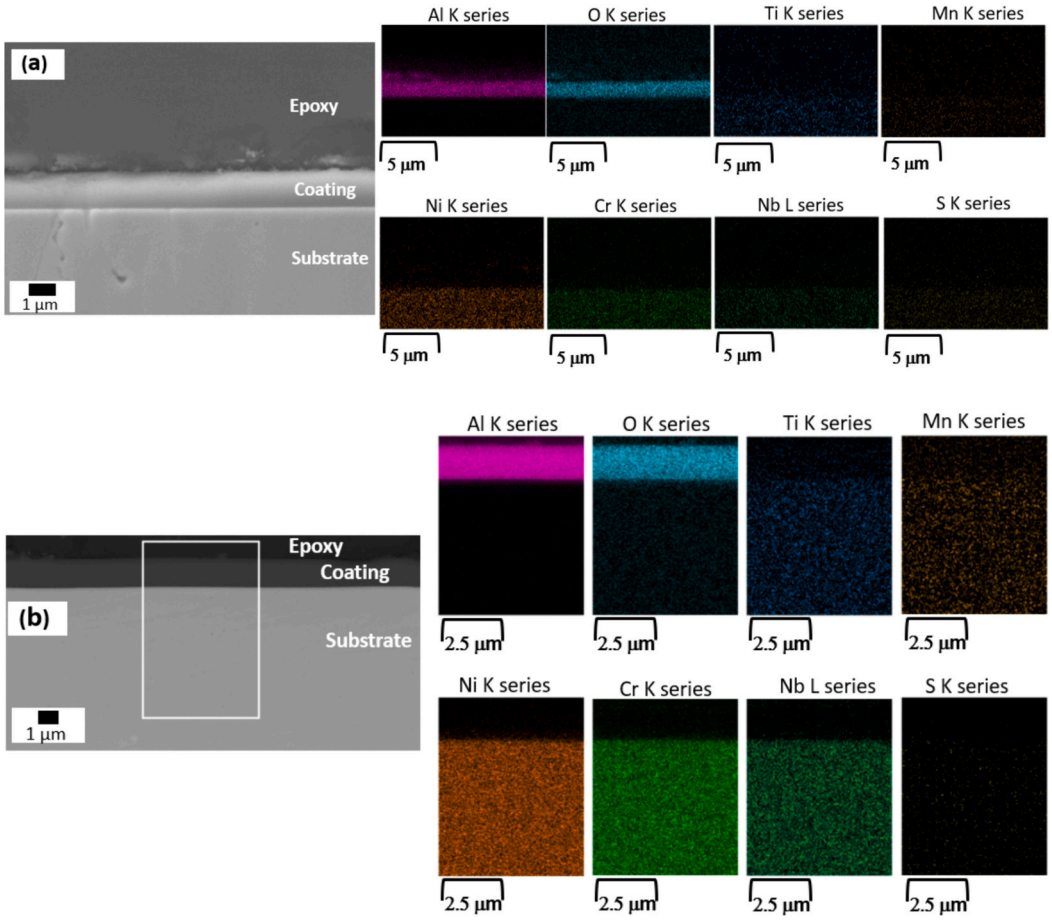


**Fig. 12.** SEM images and EDS maps on the cross-sections of as-deposited alumina on IN718 (a) and IN625 (b) after fouling at 450 °C for 2 h. The EDS of image (a) is taken from the whole area, and image (b) is taken from the highlighted rectangular area.

adherent fouling and internal oxidation were observed on the amorphous as-deposited alumina samples (Fig. 12). However, annealing introduces other oxides on the surface of the $Al_2O_3$ coating, which are less protective against fouling. The annealed surfaces accumulated coke (Fig. 9a and Fig. 10a). Conversely, the formation of TGO from the substrate material healed the coating defects, closing the short-circuit paths and enhanced the substrate protection. As a result, no internal degradation is observed in the annealed coating systems. However, after the fouling reaction, the signal of TGO on the surface is reduced in both systems (Fig. 9b and Fig. 10b), and the cracks became significantly more apparent with deeper grooves on the IN625 surface. In addition, red ellipses in Fig. 10b identify S and Ni in the same defective region, suggesting sulfidation through nickel sulfide formation on the IN625 system. Fig. 11b.2 shows a marked line from the substrate, characterizing heavier element diffusion. A red ellipse indicates nickel in that coating area, suggesting diffusion of this element. The larger grain size of IN718 compared to IN625 should minimize the substrate elemental diffusion, while increasing the protectiveness of the IN718/coating system.

The results indicate that the alumina surface effectively protects against heavy oil fouling; however, the underlying substrate plays a role in the sulfidation and coking propensity. The as-deposited alumina, due to its purity and amorphous nature, is superior in protecting against fouling when compared to alumina annealed at 1000 °C. Even though the annealed alumina has a higher hardness and adhesion that can be beneficial to avoid erosion and wear, the high-temperature annealing step may compromise the integrity of the substrates in practical applications. Therefore, when considering technological applications, one should consider the effect of the underlying substrate on the formation of pores and cracks, and how the substrate interacts with the working environment.

## 5. Conclusions

Near-stoichiometric alumina coatings reactively sputter-deposited on IN718 and IN625 interact with the substrates after annealing and protect the surface against fouling. The key findings are as follows:

1. The refractive index variation through the coating thickness is an indicator of the alumina homogeneity, while a higher homogeneity is related to enhanced adhesion. Annealing up to 1000 °C improved the adhesion on both substrates. $LC_2$ values indicate that the adhesion of alumina is initially slightly better on IN625 compared to IN718, and is the same after annealing up to 1000 °C.
2. The annealed alumina exhibits polymorphism: $\gamma$-$Al_2O_3$ prevails at 800 and 900 °C, and $\alpha$-$Al_2O_3$ is present at 1000 °C. During annealing at 1000 °C for 2 h, mainly Cr and Ti diffuse through the alumina coating, preferentially at grain boundaries and defect areas. For IN625, Mn diffusion is also detected on the surface.
3. Annealed alumina-coated IN718 showed a TGO structure on the surface, which follows grain boundaries and cracks formed in the coating. In contrast, for the alumina on IN625 samples, crater-like structures are present and no relation to the grain boundaries could be established.
4. Amorphous alumina protects against adherent fouling with no clear sign of coke or sulfidation formation. For the alumina samples annealed at 1000 °C, coke is present on the surface when IN718 is applied, while a higher degree of coke formation and possible sulfidation is detected when IN625 is used as substrate.

## CRediT authorship contribution statement

**Fellipy S. Rocha:** Writing – review & editing, Writing – original draft, Visualization, Validation, Methodology, Investigation, Formal analysis, Data curation, Conceptualization. **Etienne Bousser:** Writing – review & editing, Visualization, Validation, Project administration, Methodology, Conceptualization. **Marwan Azzi:** Writing – review & editing, Validation, Project administration. **Fadila Khelfaoui:** Writing – review & editing, Visualization, Validation, Resources, Project administration. **Luc Vernhes:** Writing – review & editing, Visualization, Validation, Resources, Project administration. **Gregory S. Patience:** Writing – review & editing, Validation, Supervision, Resources, Funding acquisition. **Jolanta E. Klemberg-Sapieha:** Writing – review & editing, Visualization, Validation, Supervision, Resources, Project administration, Funding acquisition. **Ludvik Martinu:** Writing – review & editing, Validation, Supervision, Resources, Project administration, Funding acquisition, Conceptualization.

## Declaration of competing interest

The authors declare that they have no known competing financial interests or personal relationships that could have appeared to influence the work reported in this paper.

## Data availability

Data will be made available on request.

## Acknowledgements

The authors wish to thank Mr. Francis Turcot, Mr. Francis Boutet, and Mr. Jean Ghantous for their expert technical assistance. The project was financially supported by the Natural Sciences and Engineering Research Council (NSERC) of Canada through the NSERC-Alliance grant (no. ALLRP 576758 - 22), by Prima Quebec (grant no. R24-13-003), and by Velan Inc.

## References

[1] R.C. Reed, T. Tao, N. Warnken, Alloys-by-design: application to nickel-based single crystal superalloys, Acta Mater. 57 (19) (2009) 5898–5913, https://doi.org/10.1016/j.actamat.2009.08.018.
[2] S. Patel, J. de Barbadillo, S. Coryell, Superalloy 718: evolution of the alloy from high to low temperature application, in: Proceedings of the 9th International Symposium on Superalloy 718 & Derivatives: Energy, Aerospace, and Industrial Applications, The Minerals, Metals & Materials Series, Springer International Publishing, Cham, 2018, pp. 23–49, https://doi.org/10.1007/978-3-319-89480-5_2.
[3] W. Wang, A.P. Watkinson, Iron sulphide and coke fouling from sour oils: review and initial experiments, in: Proceedings of the International Conference on Heat Exchanger Fouling and Cleaning, Crete Island, Greece, 2011, pp. 23–30.
[4] E. Diaz-Bejarano, E. Behranvand, F. Coletti, M.R. Mozdianfard, S. Macchietto, Organic and inorganic fouling in heat exchangers: industrial case study analysis of fouling rate, Ind. Eng. Chem. Res. 58 (1) (2019) 228–246, https://doi.org/10.1021/acs.iecr.8b04343.
[5] N.S. Srinivasan, C.A. McKnight, Mechanism of coke formation from hydrocracked Athabasca residuum, Fuel 73 (9) (1994) 1511–1517, https://doi.org/10.1016/0016-2361(94)90072-8.
[6] A. Kundu, K. Nigam, A.-M. Billet, H. Delmas, Recent developments on hydroprocessing reactors, Rev. Chem. Eng. 19 (6) (2003) 531–605, https://doi.org/10.1515/REVCE.2003.19.6.531.
[7] J.G. Speight, Oil and Gas Corrosion Prevention: From Surface Facilities to Refineries, Gulf Professional Publishing, Elsevier Science & Technology Books, The Boulevard, Langford Lane, Kidlington, Oxford, 2014.
[8] Nickel, cobalt, and their alloys, in: J.R. Davis, ASM International (Eds.), ASM Specialty Handbook, ASM International, Materials Park, OH, 2000.
[9] D.J. Young, Chapter 4 - mixed gas corrosion of pure metals, in: High Temperature Oxidation and Corrosion of Metals, Second edition, Elsevier, 2016, pp. 145–191, https://doi.org/10.1016/B978-0-08-100101-1.00004-2.
[10] Z.G. Yang, D.M. Paxton, K.S. Weil, J.W. Stevenson, P. Singh, Materials Properties Database for Selection of High-Temperature Alloys and Concepts of Alloy Design for SOFC Applications, PNNL-14116, 15010553, 2002, https://doi.org/10.2172/15010553.
[11] D.J. Young, Chapter 14 - alloy design, in: High Temperature Oxidation and Corrosion of Metals, Second edition, Elsevier, 2016, pp. 685–701, https://doi.org/10.1016/B978-0-08-100101-1.00014-5.
[12] R.G. Munro, S.J. Dapkunas, Corrosion characteristics of silicon carbide and silicon nitride, J Res Natl Inst Stand Technol 98 (5) (1993) 607–631, https://doi.org/10.6028/jres.098.040.
[13] D. Landolt, Corrosion and Surface Chemistry of Metals, EPFL Press, Lausanne, Switzerland, 2007.
[14] M.J. Madou, Fundamentals of Microfabrication: The Science of Miniaturization, Second edition, CRC Press, Boca Raton, 2002.
[15] I. Levin, D. Brandon, Metastable alumina polymorphs: crystal structures and transition sequences, J. Am. Ceram. Soc. 81 (8) (1998) 1995–2012, https://doi.org/10.1111/j.1151-2916.1998.tb02581.x.
[16] D.J. Young, Chapter 8 - corrosion by sulphur, in: High Temperature Oxidation and Corrosion of Metals, Second edition, Elsevier, 2016, pp. 393–430, https://doi.org/10.1016/B978-0-08-100101-1.00008-X.
[17] I. Neelakanta Reddy, V. Rajagopal Reddy, N. Sridhara, S. Basavaraja, A.K. Sharma, A. Dey, Optical and microstructural Characterisations of pulsed rf magnetron sputtered alumina thin film, Journal of Materials Science & Technology 29 (10) (2013) 929–936, https://doi.org/10.1016/j.jmst.2013.05.002.
[18] L. Landälv, Thin Film and Plasma Characterization of PVD Oxides, Department of Physics Thin Film Physics, Linköping University Electronic Press, 2017, https://doi.org/10.3384/lic.diva-134146.
[19] H.T. Kwon, et al., Sol-gel derived CeO2/α-Al2O3 bilayer thin film as an anti-coking barrier and its catalytic coke oxidation performance, AICHE J. 64 (11) (2018) 4019–4026, https://doi.org/10.1002/aic.16383.
[20] R.B. Rebak, Sulfidic corrosion in refineries – a review, Corrosion Rev. 29 (3–4) (2011), https://doi.org/10.1515/CORRREV.2011.021.
[21] A. Vencl, M. Mrdak, I. Cvijović, Microstructures and tribological properties of ferrous coatings deposited by APS (atmospheric plasma spraying) on Al-alloy substrate, FME Transactions 34 (2006) 151–157.
[22] P.P. Shetty, et al., Effect of surface chemistry and roughness on the high-temperature deposition of a model Asphaltene, Energy Fuel 33 (5) (2019) 4104–4114, https://doi.org/10.1021/acs.energyfuels.9b00386.
[23] W. Wang, A.P. Watkinson, Deposition from a sour heavy oil under incipient coking conditions: wall shear stress effects and mechanism, in: Proceedings of International Conference on Heat Exchanger Fouling and Cleaning, Enfield (Dublin), Ireland, 2015, pp. 65–73.
[24] S. Ebnesajjad, Chapter 3 - material surface preparation techniques, in: Adhesives Technology Handbook, Second edition, William Andrew Publishing, Norwich, NY, 2009, pp. 37–46, https://doi.org/10.1016/B978-0-8155-1533-3.50006-2.
[25] D.M. Mattox, Front-matter, in: Handbook of Physical Vapor Deposition (PVD) Processing, Second edition, William Andrew Publishing, Boston, 2010, pp. i–iii, https://doi.org/10.1016/B978-0-8155-2037-5.00025-3.
[26] W.C. Oliver, G.M. Pharr, An improved technique for determining hardness and elastic modulus using load and displacement sensing indentation experiments, J. Mater. Res. 7 (6) (1992) 1564–1583, https://doi.org/10.1557/JMR.1992.1564.
[27] K. Strijckmans, R. Schelfhout, D. Depla, Tutorial: hysteresis during the reactive magnetron sputtering process, J. Appl. Phys. 124 (24) (2018) 241101, https://doi.org/10.1063/1.5042084.
[28] F.C. Silva, J.C. Sagás, L.C. Fontana, J.M.C. Miscione, R.C. Cozza, C.G. Schön, 18 - Growth and properties of functionally graded ceramic coatings deposited by grid-assisted magnetron sputtering, in: R.K. Gupta, A. Motallebzadeh, S. Kakooei, T. A. Nguyen, A. Behera (Eds.), Advanced Ceramic Coatings, Elsevier Series in Advanced Ceramic Materials, Elsevier, 2023, pp. 401–432, https://doi.org/10.1016/B978-0-323-99659-4.00018-8.
[29] K. Kanaya, S. Okayama, Penetration and energy-loss theory of electrons in solid targets, J. Phys. D Appl. Phys. 5 (1) (1972) 43–58, https://doi.org/10.1088/0022-3727/5/1/308.
[30] M. Nofz, I. Dörfel, R. Sojref, R. Saliwan Neumann, Microstructure of bare and sol–gel alumina-coated nickel-base alloy inconel 625 after long-term oxidation at 900 °C, Oxid Met 91 (3) (2019) 395–416, https://doi.org/10.1007/s11085-019-09888-z.
[31] J.M. Andersson, E. Wallin, U. Helmersson, U. Kreissig, E.P. Münger, Phase control of Al2O3 thin films grown at low temperatures, Thin Solid Films 513 (1) (2006) 57–59, https://doi.org/10.1016/j.tsf.2006.01.016.
[32] Y. Zhao, Y. Qian, W. Yu, Z. Chen, Surface roughness of alumina films deposited by reactive r.f. sputtering, Thin Solid Films 286 (1) (1996) 45–48, https://doi.org/10.1016/S0040-6090(95)08514-9.
[33] M. Dressler, M. Nofz, I. Dörfel, R. Saliwan-Neumann, Diffusion of Cr, Fe, and Ti ions from Ni-base alloy inconel-718 into a transition alumina coating, Thin Solid Films 520 (13) (2012) 4344–4349, https://doi.org/10.1016/j.tsf.2012.02.006.
[34] M. Dressler, M. Nofz, I. Dörfel, R. Saliwan-Neumann, Influence of sol–gel derived alumina coatings on oxide scale growth of nickel-base superalloy Inconel-718, Surf. Coat. Technol. 202 (24) (2008) 6095–6102, https://doi.org/10.1016/j.surfcoat.2008.07.018.
[35] D.M. Gorman, R.L. Higginson, H. Du, G. McColvin, A.T. Fry, R.C. Thomson, Microstructural analysis of IN617 and IN625 oxidised in the presence of steam for use in ultra-supercritical power plant, Oxid Met 79 (5) (2013) 553–566, https://doi.org/10.1007/s11085-012-9342-2.
[36] R.P. Oleksak, C.S. Carney, G.R. Holcomb, Ö.N. Doğan, Structural evolution of a Ni alloy surface during high-temperature oxidation, Oxid Met 90 (1) (2018) 27–42, https://doi.org/10.1007/s11085-017-9821-6.
[37] A.K. Krella, Chapter 16 - Degradation of protective PVD coatings, in: A.S. H. Makhlouf, M. Aliofkhazraei (Eds.), Handbook of Materials Failure Analysis with Case Studies from the Chemicals, Concrete and Power Industries, Butterworth-

Heinemann, 2016, pp. 411–440, https://doi.org/10.1016/B978-0-08-100116-5.00016-8.
[38] M. Abdoos, B. Bose, S. Rawal, A.F.M. Arif, S.C. Veldhuis, The influence of residual stress on the properties and performance of thick TiAlN multilayer coating during dry turning of compacted graphite iron, Wear 454–455 (2020) 203342, https://doi.org/10.1016/j.wear.2020.203342.
[39] Kh.A. Al-hatab, M.A. Al-bukhaiti, U. Krupp, M. Kantehm, Cyclic oxidation behavior of IN 718 Superalloy in air at high temperatures, Oxid. Met. 75 (3) (2011) 209–228, https://doi.org/10.1007/s11085-010-9230-6.
[40] A.M. de Sousa Malafaia, R.B. de Oliveira, L. Latu-Romain, Y. Wouters, R. Baldan, Isothermal oxidation of Inconel 625 superalloy at 800 and 1000 °C: microstructure and oxide layer characterization, Mater Charact 161 (2020) 110160, https://doi.org/10.1016/j.matchar.2020.110160.
[41] L. Boatemaa, C. Kwakernaak, S. van der Zwaag, W.G. Sloof, Selection of healing agents for autonomous healing of alumina at high temperatures, J. Eur. Ceram. Soc. 36 (16) (2016) 4141–4145, https://doi.org/10.1016/j.jeurceramsoc.2016.05.038.
[42] G.R. Holcomb, D.E. Alman, The effect of manganese additions on the reactive evaporation of chromium in Ni–Cr alloys, Scr. Mater. 54 (10) (2006) 1821–1825, https://doi.org/10.1016/j.scriptamat.2006.01.026.
[43] P. Bowen, C. Carry, From powders to sintered pieces: forming, transformations and sintering of nanostructured ceramic oxides, Powder Technol. 128 (2) (2002) 248–255, https://doi.org/10.1016/S0032-5910(02)00183-3.
[44] J. Musil, J. Blažek, P. Zeman, Š. Prokšová, M. Šašek, R. Čerstvý, Thermal stability of alumina thin films containing γ-Al2O3 phase prepared by reactive magnetron sputtering, Appl. Surf. Sci. 257 (3) (2010) 1058–1062, https://doi.org/10.1016/j.apsusc.2010.07.107.
[45] X. Tang, Effects of the annealing heating rate on sputtered aluminum oxide films, J. Wuhan Univ. Technol.-Mat. Sci. Edit. 32 (1) (2017) 94–99, https://doi.org/10.1007/s11595-017-1565-2.
[46] M. Dressler, M. Nofz, R. Saliwan-Neumann, I. Dörfel, M. Griepentrog, Sol–gel derived alumina layers on nickel-base superalloy Inconel-718 (IN-718), Thin Solid Films 517 (2) (2008) 786–792, https://doi.org/10.1016/j.tsf.2008.08.124.
[47] T. Connolley, P.A.S. Reed, M.J. Starink, Short crack initiation and growth at 600°C in notched specimens of Inconel718, Mater. Sci. Eng. A 340 (1) (2003) 139–154, https://doi.org/10.1016/S0921-5093(02)00169-7.
[48] N. Birks, G.H. Meier, F.S. Pettit, High-temperature corrosion resistance, JOM 39 (12) (1987) 28–31, https://doi.org/10.1007/BF03257568.